AIAA JOURNAL
Vol. 43, No. 12, December 2005

Numerical Investigation of Low-Pressure Turbine Blade Separation Control

A. Gross* and H. F. Fasel†
University of Arizona, Tucson, Arizona 85721

Laminar separation on the suction side of low-pressure turbine (LPT) blades at low operating Reynolds numbers can degrade overall engine efficiency and impose limitations on the flight envelope. In wind-tunnel experiments it was shown that laminar separation can be controlled by pulsed vortex generator jets. This active-flow-control technology could be transferred to real flight hardware with more confidence if the physical mechanisms involved in the control were better understood. Here, calculations of a linear LPT cascade at a Reynolds number based on axial chord of 2.5×10^4 are presented and compared to experimental data. Good agreement was observed between numerical and experimental results, except in the separated region near the trailing edge. In two-dimensional calculations separation was controlled by pulsed blowing through a slot upstream of the flow separation location. The blade pitch was then increased by 25% to obtain a larger region of separated flow. Again, using pulsed blowing through a slot, the separation could be controlled, and an increase of 19% in the time-averaged ratio of lift and drag was achieved.

Nomenclature

a,A	=	Fourier mode amplitude
B	=	blowing ratio
b	=	slot width
C_x	=	axial chord
c	=	coefficient, speed of sound
d	=	blade spacing in y
e	=	total energy
$\boldsymbol{F}$	=	flux vector
F^+	=	nondimensional forcing frequency
f	=	forcing function, nondimensional frequency
J	=	Jacobian
M	=	Mach number
Pr	=	Prandtl number
p	=	pressure
Q	=	vortex identification criterion
$\boldsymbol{Q}$	=	state vector
R	=	residual
Re	=	Reynolds number
S	=	strain tensor
T	=	temperature, period
t	=	time
V	=	contravariant velocity
v	=	velocity
W	=	rotation tensor
x	=	physical coordinate
γ	=	ratio of specific heats
ε	=	internal energy
κ	=	heat conductivity
μ	=	viscosity
ξ	=	curvilinear coordinate
ρ	=	density
τ	=	stress, duty cycle
ω_z	=	spanwise vorticity

Subscripts

i, j, k	=	coordinate
tot	=	total
x	=	in axial direction
y	=	normal to axial direction
μ	=	momentum
∞	=	inflow

Superscript

v	=	viscous

Introduction

LOW-PRESSURE turbine (LPT) stages are important components of many modern jet engines. In the recent past, unmanned aerial vehicles (UAVs) have become increasingly important for military and civil operations. One direction in the development of UAVs is the trend toward smaller vehicles and therefore smaller jet engines. Small inflow velocities and/or blade dimensions can lead to low operating Reynolds numbers and cause boundary layers to remain essentially laminar, even in the presence of elevated freestream turbulence. Laminar separation can occur, causing significant losses in turbine and overall engine performance. Because off-design conditions are often unavoidable, conservative design margins have to be adopted in the design of LPT stages to guarantee safe and reliable operation. An on-demand active-flow-control (AFC) system that would assist during critical off-design operation and that can be deactivated during cruise flight conditions would be beneficial. A different strategy could be to reduce the blade count (and thus component weight) and avoid separation in all flight conditions, including cruise, by continuously applying AFC.

It was recognized several years ago that AFC applied to LPT blades can control laminar separation and lead to considerable performance improvements. In an extensive experimental research program at the Air Force Research Laboratory (AFRL) at Wright–Patterson Air Force Base, Rivir and coworkers (see Refs. 1–5) systematically investigated the benefits of AFC with vortex generator jets (VGJs) for a linear PakB LPT cascade. Bons et al.[2] showed that the momentum deficit at off-design conditions could be reduced by more than 50% using pulsed VGJs. Sondergaard et al.[4,5] were able to control separation at a 50% larger blade spacing. Although the experiments at AFRL by Rivir and coworkers have convincingly demonstrated the potential benefits of AFC using VGJs, the relevant physical mechanisms are far from understood. Fundamental questions why VGJs are so effective in preventing separation or reattaching

Received 5 March 2003; revision received 2 March 2005; accepted for publication 8 May 2005.

*Research Associate, Department of Aerospace and Mechanical Engineering. Member AIAA.

†Professor, Department of Aerospace and Mechanical Engineering. Member AIAA.

separated boundary layers for LPT blades have yet to be answered. The underlying physics are highly complex, as both unsteady separation and transition mechanisms are at work interactively. For LPT applications, as a consequence of the hydrodynamic instability of the separating boundary layer, disturbance waves amplify strongly in the streamwise direction and quickly reach very large amplitudes. The strong amplification is caused by the streamwise adverse pressure gradient, the convex wall curvature (suction side of blade), and of course the inviscid instability mechanism when the boundary layer is separating. Because of the elevated freestream turbulence, breakdown to turbulence is typically caused by "bypass" mechanisms.[6] Because of the nonlinearity and the nonuniqueness of the bypass mechanisms, slight changes in "initial" conditions (operating conditions) can result in drastically different breakdown-to-turbulence scenarios. The fundamental understanding of separation is almost as incomplete as that of transition, especially when the separation process is unsteady and three dimensional as in the application investigated here. The unsteadiness is introduced by the pulsing of the VGJs, by the naturally present large "coherent" flow structures, which result from the instability of the separated laminar boundary layer, and, in the real application, by the periodically passing wakes of the upstream blades. Thus it is obvious for LPTs that transition and separation interact in a very complex manner. When frequencies and amplitudes of the pulsed blowing are "just right," the effectiveness of separation control is indeed stunning, requiring a very small energy input. In other instances AFC is not effective in the sense that separation is not prevented or significantly delayed or that an unacceptable energy input is required. Therefore, we believe that a better understanding of the most relevant physical mechanisms needs to be achieved before this technology can be transitioned successfully into practice and to ensure safe, reliable, and effective operation.

Numerous experimental studies of separation on LPT blades clearly demonstrate the potential benefits of flow control. Lake et al.[7] reported on investigations involving modified blade surfaces (dimples) and concluded that boundary-layer separation was significantly reduced. However, a disadvantage of such passive techniques is increased viscous losses at conditions where unmodified (uncontrolled) blades yield satisfactory turbine performance. Extensive experimental studies of active LPT separation control were conducted by Bons et al.[1–3] and Sondergaard et al.[4,5] using steady and pulsed VGJs and by Huang et al.[8] using steady and pulsed plasma actuators. In these experiments a drastic reduction in boundary-layer separation on the suction side of the LPT blade was achieved. Pulsed actuation was shown to be much more efficient than steady actuation and to require a lower energy input. The significant impact of pulsed VGJ control on the separation behavior was attributed to triggering of early boundary-layer transition, especially when the jets were employed near the natural separation location. The effectiveness of steady blowing was attributed mainly to freestream momentum entrainment resulting from the generated longitudinal vortices.

In addition to experimental investigations, numerical simulations of LPT flows were performed by several research groups. Two-dimensional and three-dimensional implicit large-eddy simulations (ILES) of the PakB cascade at three different Reynolds numbers were carried out by Rizzetta and Visbal[9,10] using a high-order-accurate compressible code. The computational grid used for the three-dimensional simulations of the "natural," uncontrolled flow had 6.5 million grid points. For investigations of AFC by pulsed VGJs, an embedded grid was placed over the VGJ holes to increase local grid resolution, resulting in a total of 18.6 million grid points. For $Re = 2.5 \times 10^4$, flow separation was predicted at $\approx 0.73 C_x$ (C_x is the axial chord length). In the three-dimensional simulation the flow transitioned close to the trailing edge. Flow reattachment was observed at $0.97 C_x$ in the two-dimensional calculation and $0.85 C_x$ in the three-dimensional simulation. Because of the earlier reattachment in the three-dimensional simulation, the pressure recovery was stronger than in the two-dimensional calculations. The same geometry at $Re = 2.5 \times 10^4$ was also investigated numerically by the present authors.[11–13] Using two-dimensional simulations, flow separation was seen at $\approx 0.7 C_x$. The separation could be successfully controlled by pulsed blowing through a slot. A two-dimensional calculation for the same case ($Re = 2.5 \times 10^4$) using a high-order-accurate compressible code was performed by Mutnuri et al.[14] Flow separation was predicted at $0.71 C_x$. All of the numerical simulations mentioned here (except for the three-dimensional ILES) reported flow separation slightly farther downstream than in the experiments by Rivir and coworkers[1–5] and Huang et al.[8] Possible reasons for this consistent discrepancy are still being discussed. In the experiments the flow separated at $\approx 0.7 C_x$ (which roughly corresponds to the beginning of uncovered turning) and reattached at $\approx 0.99 C_x$ for an inflow turbulence level of 1%. For an inflow turbulence level of 4%, the respective locations were $\approx 0.75 C_x$ and $\approx 0.88 C_x$. The latter numbers compare well with the three-dimensional ILES results by Rizzetta and Visbal[9] for zero freestream turbulence.

Raverdy et al.[15] performed an ILES of the T106 LPT blade in a linear cascade at $Re = 11 \times 10^4$. The code was second-order accurate and based on the compressible Navier–Stokes equations in a finite volume formulation. The largest computational grid had two million grid points. Mean velocity profiles and wall-pressure distribution of the experiment were matched. A large-eddy simulation (LES) of the same geometry at a Reynolds number of 58.1×10^3 with 10.6 million grid points was carried out by Michelassi et al.[16] They used the incompressible Navier–Stokes equations with a second-order-accurate finite volume formulation and a dynamic subgrid-stress model. The transition of the laminar boundary layer on the suction side by periodic upstream wakes and the appearance of longitudinal vortices on the pressure side were studied. The same blade geometry at a higher Reynolds number of 14.8×10^4 was also studied by Xiaohua and Durbin.[17] They used a second-order-accurate incompressible code and performed simulations with up to 57 million grid points. The focus of this investigation was on the formation of longitudinal vortices on the pressure side of the blades caused by the passage of time-periodic upstream wakes. Suzen and Huang[18] developed an intermittency model to more cost effectively study the wake/blade interaction. Results for the PakB cascade at a Reynolds number of 5×10^4 were obtained using an incompressible second-order-accurate code.

This paper is organized as follows: After a description of the numerical method, two- and three-dimensional simulations of the LPT blade geometry used by Rivir and coworkers (see Refs. 1–5) are presented. Simulations were carried out for both the design blade spacing and for a 25% larger blade spacing. Because three-dimensional simulations of the full cascade are very expensive, they are not feasible for AFC parameter studies. Two-dimensional calculations are less costly and hence better suited for exploring the parameter space (e.g., amplitude, frequency, actuator location) for controlling separation using AFC. Therefore, AFC by pulsed blowing through a slot was investigated in two-dimensional calculations for both blade spacings.

Computational Approach

Governing Equations

The compressible Navier–Stokes equations in curvilinear coordinates ξ_i ($i = 1, 2, 3$) and conservation form are

$$J \frac{\partial \boldsymbol{Q}}{\partial t} + \frac{\partial \boldsymbol{F}_i}{\partial \xi_i} - \frac{1}{Re} \frac{\partial \boldsymbol{F}_i^v}{\partial \xi_i} = 0 \tag{1}$$

The equations are nondimensionalized by axial chord C_x, cascade inflow velocity v_∞, density ρ_∞, and viscosity μ_∞. $Re = \rho_\infty v_\infty C_x / \mu_\infty$ is the Reynolds number, and J is the transformation Jacobian from physical x_i ($i = 1, 2, 3$) to curvilinear coordinates ξ_i. The state vector is

$$\boldsymbol{Q} = [\rho \quad \rho v_1 \quad \rho v_2 \quad \rho v_3 \quad \rho e]^T \tag{2}$$

with velocities v_i in x_i direction, density ρ, and total energy $e = \varepsilon + \frac{1}{2} v_i v_i$. The gas is assumed to be perfect

$$p = \rho T / \gamma M^2 \tag{3}$$

with static pressure p, temperature T, isentropic exponent $\gamma = 1.4$, and inflow Mach number $M = v_\infty / c_\infty$. The local speed of sound

is $c=\sqrt{T}/M$, and the internal energy $\varepsilon=T/[\gamma(\gamma-1)M^2]$. The convective flux vectors are

$$\boldsymbol{F}_i=\begin{bmatrix}\rho V_i\\ \rho v_1 V_i+\xi_{i,1}p\\ \rho v_2 V_i+\xi_{i,2}p\\ \rho v_3 V_i+\xi_{i,3}p\\ (\rho e+p)V_i\end{bmatrix} \tag{4}$$

with contravariant velocity

$$V_i=\xi_{i,j}v_j \tag{5}$$

The viscous flux vectors are

$$\boldsymbol{F}_i^v=\begin{bmatrix}0\\ f_{1i}\\ f_{2i}\\ f_{3i}\\ v_j f_{ji}+\kappa\xi_{i,j}T_{,j}\end{bmatrix} \tag{6}$$

with $f_{ji}=\xi_{i,k}\tau_{jk}$ and stress tensor

$$\tau_{jk}=2\mu\left(S_{jk}-\tfrac{1}{3}v_{i,i}\delta_{jk}\right) \tag{7}$$

The inner derivatives of $T_{,j}$ (and analogously $v_{i,j}$) are

$$T_{,j}=\frac{\partial T}{\partial x_j}=\frac{1}{J}\xi_{i,j}\frac{\partial T}{\partial \xi_i} \tag{8}$$

and the strain rate tensor is

$$S_{ij}=\tfrac{1}{2}(v_{i,j}+v_{j,i}) \tag{9}$$

For the dependence of the laminar viscosity μ on temperature, the Sutherland law is employed. The thermal conductivity is obtained from the Prandtl analogy $\kappa=\mu/[Pr(\gamma-1)M^2]$ using a constant Prandtl number $Pr=0.72$.

Numerical Method

The numerical method for solving the governing equations was designed as a hybrid of a finite volume and a finite difference method. The convective terms are discretized with a ninth-order-accurate upwind scheme based on a weighted essentially nonoscillatory (WENO) extrapolation of the characteristic variables and the Roe scheme.[19] Because high-order-accurate finite volume formulations of the viscous terms are very cumbersome, it was decided to only transfer the convective terms into the finite volume formulation and retain the viscous terms in the finite difference formulation. Fourth-order-accurate finite differences are used for the viscous terms, and a second-order-accurate Adams–Moulton method is employed for an implicit time integration. The resulting system of equations is solved iteratively by a Newton iteration based on a line Gauss–Seidel algorithm. The convergence of the iteration method is monitored by using the residual $\boldsymbol{R}$ (with individual elements R_m) of Eq. (1). An overall maximum residual can be defined by averaging the elements R_m over all cells N and taking the maximum

$$R=\max_m\left(\sqrt{\frac{1}{N}\sum_N R_m^2}\right) \tag{10}$$

Boundary Conditions

Velocities and temperature are prescribed at the inflow boundary, while the static pressure is extrapolated from the interior to allow upstream traveling acoustic waves to leave the computational domain. At the outflow boundary the static pressure is prescribed while temperature and velocities are extrapolated. The no-slip condition is applied at the wall except at the forcing slot used for AFC where a forcing velocity is prescribed. The wall is treated as adiabatic. Periodicity conditions are employed at all other boundaries.

Table 1 Block grid sizes for two-dimensional LPT simulations

Block	Coarse grid	Fine grid
1	20×30	20×30
2	20×20	20×20
3	300×70	500×100
4	150×50	260×100
5	70×30	130×110

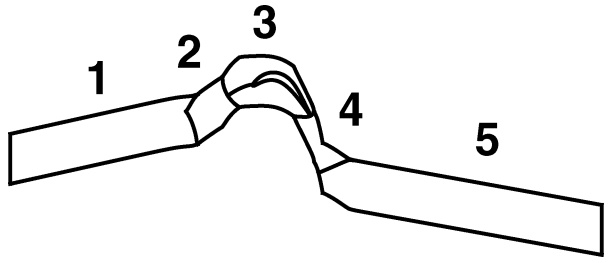

a)

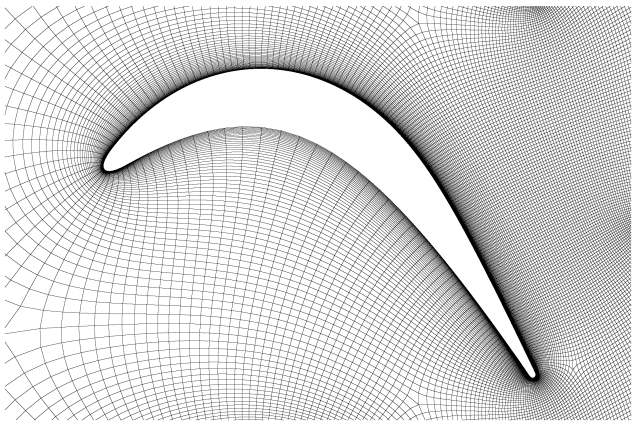

b)

Fig. 1 Computational grid for LPT simulations for design blade spacing: a) block structure and b) close-up of block 3 (fine grid, every other line shown).

Computational Grid

The computational grids used for the turbine-blade simulations consisted of five blocks (Fig. 1). Because periodicity was prescribed, only one blade needed to be computed to simulate a cascade with an infinite number of blades. Grid points were concentrated in the expected separated flow region on the suction side of the blade. The grid was stretched strongly in streamwise direction near the inflow and outflow boundaries in order to dampen upstream and downstream traveling disturbance waves. The block grid sizes used for the turbine-blade simulations are listed in Table 1. For the three-dimensional simulations 64 cells were used in spanwise direction. As in the numerical studies by Rizzetta and Visbal,[9] the spanwise grid extent was set to $0.2C_x$. The grid resolution on the suction side in wall units based on the flow state at midchord on the suction side was $x^+=2\ldots25$, $y^+=0.05\ldots1$, and $z^+=9.4$ for the design blade spacing and $x^+=2\ldots20$, $y^+=0.1\ldots1$, and $z^+=9.4$ for the 25% larger blade spacing. Rizzetta and Visbal[9] used $x^+=3.1\ldots50.6$, $y^+=0.4$, and $z^+=6.5$. These resolutions can still seem coarse for direct numerical simulations. However, according to Margolin and Rider,[20] the WENO upwind finite volume approach used for the present simulations should exhibit similar diffusion characteristics as standard (Smagorinsky type) subgrid-scale turbulence models used in LES. Thus, the present three-dimensional simulations can be considered as ILES. However, the ILES properties have to be investigated in more detail.

Results

For the results presented in this paper, the $Re=2.5\times10^4$ case from the experiments by Rivir and coworkers (see Refs. 1–5) was

chosen. This case was most susceptible to laminar separation. The inflow Mach number in the experiments was 0.0064. For the results presented here, the inflow Mach number was raised to 0.1 to accelerate the convergence of the numerical method. The same inflow Mach number was chosen also by Rizzetta and Visbal[9] for their simulations. In a separate investigation (omitted here) it was shown that compressibility effects played an insignificant role for Mach numbers of $M = 0.1$ or smaller. The experimental cascade had an inflow angle of 55 deg and a design exit angle of 30 deg (both measured from the plane of the cascade). The ratio of blade spacing d and axial chord C_x was 0.88 for the original cascade of Rivir and coworkers (see Refs. 1–5) and 1.1 for the cascade with 25% larger blade spacing.[5] The experimental cascade consisted of eight blades with a span of $\approx 5C_x$. In our simulations, both the number of blades and the span were assumed to be infinite (using periodicity conditions). All cases were computed with a nondimensional time step of $\Delta t = 0.001$ and a convergence criterion $R = 1$ [Eq. (10)]. The Courant–Friedrichs–Lewy number was about 430 at the design blade spacing and 350 at the 25% larger blade spacing. This resulted in about 20–30 iterations per time step for the implicit method.

For the two-dimensional calculations with AFC, a forcing slot was positioned upstream of the separation (between $0.645 \le x/C_x \le 0.655$ for the design blade spacing and between $0.573 \le x/C_x \le 0.583$ for the 25% larger blade spacing). The slot width was $b = 0.01C_x$. Oscillatory wall-normal blowing with velocity $Bv_\infty f(t)$ was applied over the entire slot width. The blowing ratio B is defined as the ratio of the blowing velocity to the cascade inflow velocity v_∞. The nondimensional forcing frequency F^+ is nondimensionalized with inflow velocity v_∞ and chord C_x. The nondimensional period T is defined as its inverse. In the experiments by Rivir and coworkers (see Refs. 1–5), it was found that forcing with a reduced duty cycle (Fig. 2) resulted in a very effective flow control. Therefore, in the simulations we also chose a square forcing function:

$$f(t) = \begin{cases} 1 & \text{if} \quad 0 \le t \le \tau T \\ 0 & \text{if} \quad \tau T < t < T \end{cases} \tag{11}$$

$$f(t+T) = f(t) \tag{12}$$

The duty cycle τ is defined as the ratio of jet on time and forcing period T. The forcing function $f(t)$ can be Fourier decomposed:

$$f(t) = \frac{a_0}{2} + \sum_n a_n \cos\left[\frac{2\pi}{T} n(t - 0.5\tau T)\right] \tag{13}$$

with Fourier mode amplitudes

$$a_0 = \tau \tag{14}$$

$$a_n = (2/\pi n)\sin \pi n\tau \tag{15}$$

and frequencies $f_n = n/T$. The Fourier mode amplitudes for different duty cycles τ and forcing frequencies F^+ are shown in Fig. 3. As

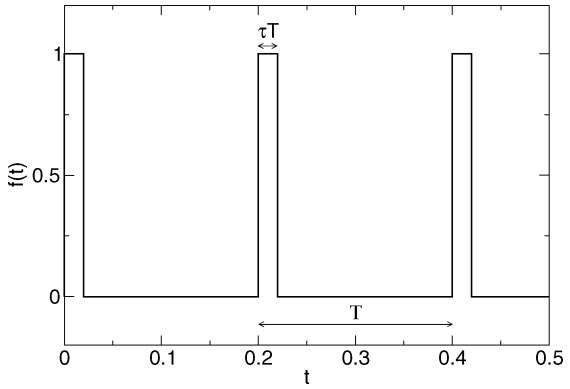

Fig. 2 Reduced duty cycle forcing function with period $T = 0.4$ and duty cycle $\tau = 0.1$.

Table 2 Total computation times Δt until beginning of time averaging (startup) and for obtaining time-averaged data (averaging)

	$d/C_x = 0.88$		$d/C_x = 1.1$	
F^+	Startup	Averaging	Startup	Averaging
Natural	6	6	6	12
2.5	6	3	6	9
3.33	6	3	9	3
4	—	—	6	6
5	6	6	6	9
6.67	—	—	9	6
10	6	3	6	6

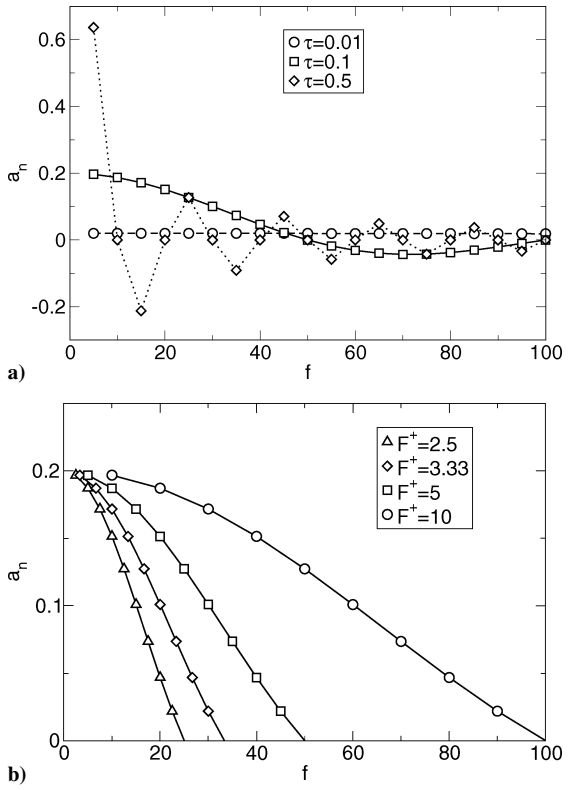

Fig. 3 Fourier decompositions of square forcing functions for a) three different duty cycles τ and fixed forcing frequency $F^+ = 5$ and b) four different forcing frequencies F^+ and fixed duty cycle $\tau = 0.1$.

the duty cycle is lowered, the frequency spectrum becomes flatter (Fig. 3a), and the individual mode amplitudes become smaller. As the duty cycle approaches very small values, the amplitude drop-off toward shorter periods (or alternatively higher frequencies) becomes smaller, meaning that for smaller duty cycles higher harmonics are forced at comparatively larger amplitudes. Also noteworthy is that for a duty cycle $\tau = 0.5$ only uneven multiples of F^+ are forced. For $\tau = 0.1$ modes $n = 10, 20, \ldots$ are zero. Arguably, a perfect square forcing function can never be achieved in the experiment. However, the square forcing function used in the experiments by Rivir and coworkers (see Refs. 1–5) can exhibit similar properties.

In the experiments[1–5] blowing ratios in the range of 1 to 4 and duty cycles in the range of 1 to 50% were explored. For the controlled cases presented in this paper, a blowing ratio of $B = 1$ and a duty cycle of $\tau = 10\%$ were chosen. Forcing frequency spectra for this duty cycle and four different forcing frequencies F^+ are shown in Fig. 3b. The momentum coefficient

$$c_\mu = (b/C_x)\tau B^2 \tag{16}$$

was 10^{-3}.

All two-dimensional simulations were first run for a certain startup duration before time averages were computed to prevent startup transients from influencing the time-averages (Table 2). Once

the flow was observed to become periodic in time, the time averaging was started. The three-dimensional simulations were computed for a duration $\Delta t = 2.7$ (design blade spacing) and $\Delta t = 2.1$ (25% larger blade spacing). Only instantaneous results are shown for the three-dimensional cases because time averages were not computed.

The aerodynamic forces in axial direction F_x and normal to the axial direction F_y were computed by integrating the pressure and friction forces over the entire blade surface. The aerodynamic coefficients in x and y direction were then obtained by nondimensionalizing the aerodynamic forces using the inflow dynamic pressure, the chord C_x, and the unit span

$$c_{x,y} = F_{x,y} \Big/ C_x \tfrac{1}{2} \rho_\infty v_\infty^2 \tag{17}$$

Design Blade Spacing

Instantaneous contours of the spanwise vorticity obtained from a two-dimensional calculation at the design blade spacing $d/C_x = 0.88$ are shown in Fig. 4. The boundary layer separates at $x \approx 0.73 C_x$. The separated shear layer is inviscidly unstable. Small disturbances are exponentially amplified to nonlinear, large amplitudes, forming spanwise vortices that travel in downstream direction and facilitate mixing with the surrounding high-momentum fluid. This entrainment of high-momentum freestream fluid aids flow reattachment, in this case upstream of the trailing edge. Downstream of the trailing edge of the blade, the spanwise structures interact with the counter-rotating vorticity originating from the pressure side of the blade. The trailing wake is dominated by the shedding frequency associated with the instability of the separated shear layer and its lower and higher harmonics.

Time-averaged curves for the wall-pressure coefficient

$$c_p = \frac{p - p_\infty}{\frac{1}{2} \rho_\infty v_\infty^2} \tag{18}$$

are shown in Fig. 5. Also included in Fig. 5 are measurements by Rivir and coworkers (see Refs. 1–5) and Huang et al.,[8] as well as results from a three-dimensional ILES by Rizzetta and Visbal.[9] The upper part of the graph represents the suction side of the blade, the lower part the pressure side. In both experiments the inflow turbulence level was about 1% (Refs. 1–5 and 8). Compared to the experiments, the numerical results show a somewhat later separation and a slightly higher pressure plateau in the separated region. This discrepancy has been noticed in previous studies.[11,12] The "hump" near the trailing edge in the c_p distributions of the two-dimensional calculations is not visible in the three-dimensional ILES (Fig. 5). It appears to be an "artifact" of strong two-dimensional (spanwise) coherent structures. These structures facilitate a large momentum exchange in wall-normal direction leading to early flow reattachment. In three-dimensional simulations the flow is allowed to transition. The eddy viscosity introduced by small-scale turbulent structures weakens the coherence of the two-dimensional structures thereby delaying reattachment.[21] Also included in Fig. 5 are results obtained on the coarser grid and with different iteration convergence criteria. Fine-grid results are shown for two iteration convergence criteria, $R = 1$ and 0.01. The $R = 0.01$ calculations required about 80–90 iterations per time step. The results are sufficiently close to each other to justify the use of $R = 1$ for the calculations discussed next. Also, the coarse-

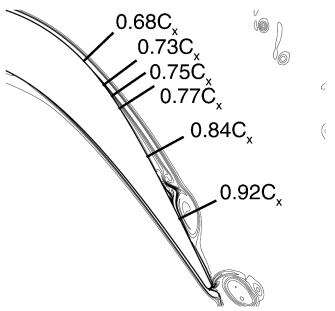

Fig. 4 Isocontours of instantaneous spanwise vorticity ω_z and locations where time-averaged velocity profiles were taken: natural (uncontrolled) flow, design blade spacing.

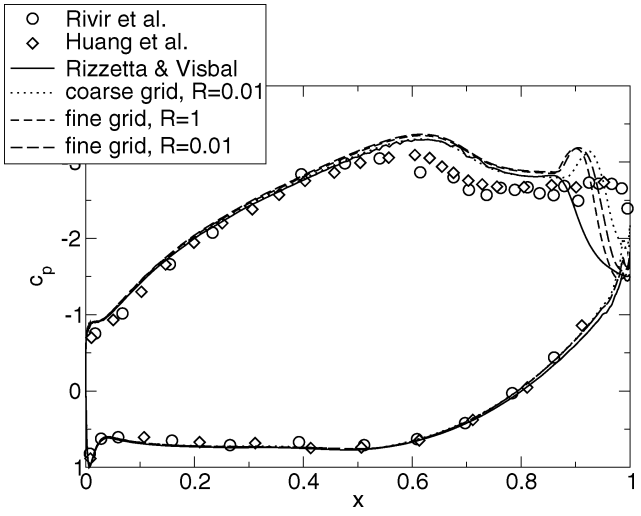

Fig. 5 Time-averaged wall-pressure coefficient: natural (uncontrolled) flow, design blade spacing.

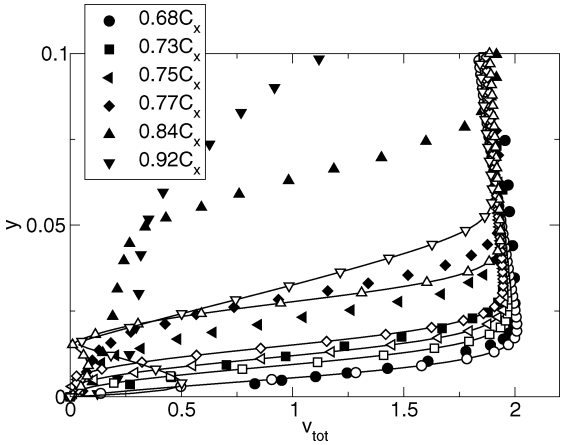

Fig. 6 Time-averaged wall-normal velocity profiles at six different downstream stations on the suction side (see Fig. 4): filled symbols, measurements by Rivir and coworkers and open symbols, results obtained from two-dimensional calculation; natural (uncontrolled) flow, design blade spacing.

and the fine-grid results for $R = 0.01$ are close to each other. The coarse-grid solution shows a weaker hump closer to the trailing edge, indicating slightly weaker structures. The difference is however minor, and therefore the fine grid was considered to be sufficient.

In Fig. 6, velocity profiles at various streamwise locations obtained from the two-dimensional calculation are compared to those from the experiments by Rivir and coworkers (see Refs. 1–5). At 68% axial chord, the profiles match well. At all other stations, the measured velocity profiles differ significantly from the computed profiles, however, mainly because of the fact that the experiments exhibit a larger separation bubble than the simulations, as already addressed.

A visualization of instantaneous data obtained from a three-dimensional simulation is shown in Fig. 7. For this picture the integration domain was repeated once in spanwise direction so that the developing flow structures can be observed better. Shown in Fig. 7 are isosurfaces of the Q criterion[22]

$$Q = \tfrac{1}{2}(W_{ij} W_{ij} - S_{ij} S_{ij}) \tag{19}$$

where $W_{ij} = \frac{1}{2}(v_{i,j} - v_{j,i})$ is the rotation tensor. A positive Q criterion indicates areas where rotation dominates strain. The two-dimensional spanwise structures that periodically develop as a consequence of the shear-layer instability become unstable with respect to three-dimensional disturbances. These disturbances initially

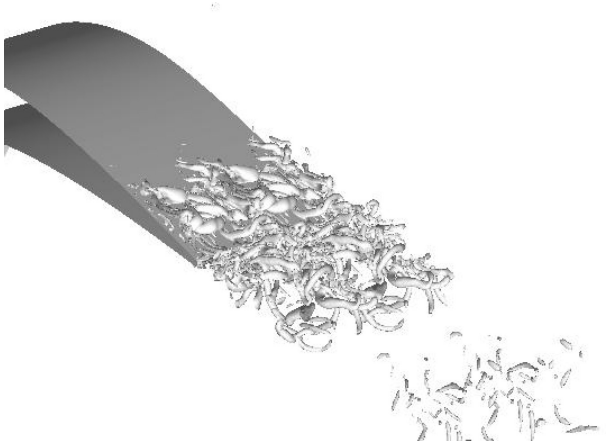

Fig. 7 Isosurface of $Q = 1000$ for three-dimensional simulation: perspective view in upstream direction, design blade spacing.

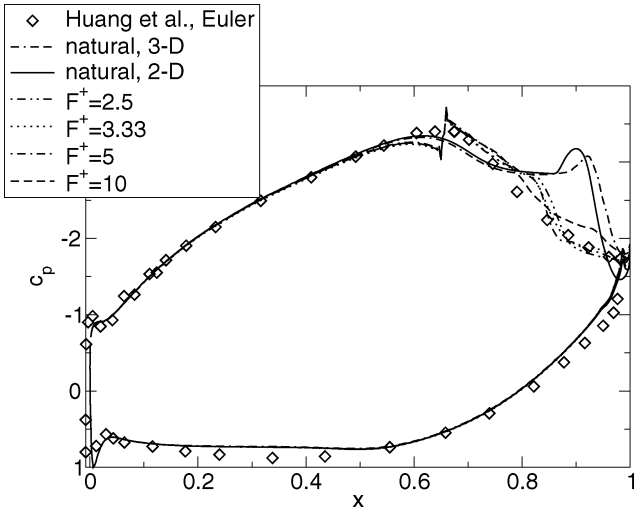

Fig. 8 Time-averaged wall-pressure coefficient: design blade spacing.

cause a three-dimensional modulation of the two-dimensional structures and eventually lead to a rapid breakdown to turbulence upstream of the trailing edge. Although the wake is turbulent, the unsteady footprints of the two-dimensional shear-layer instability can still be recognized by the presence of distinct spanwise coherent structures in the wake. Their strength is, however, diminished by the turbulent mixing when compared to the two-dimensional simulations. The strong two dimensionality of the flow over most of the blade explains why the c_p curves for the two- and the three-dimensional cases shown in Fig. 8 are relatively similar. The additional diffusion caused by the turbulent mixing weakens the spanwise structures. The hump in the c_p curve is diminished somewhat and shifted in downstream direction. A similar trend could be observed in the two-dimensional calculations when additional numerical diffusion was introduced by computing on the coarser grid (Fig. 5). Because the difference between the two- and three-dimensional result is small and because three-dimensional simulations are prohibitively expensive, it was decided to perform all AFC investigations using two-dimensional calculations only. This, of course, excluded investigations of discrete VGJs.

For our investigations of AFC using oscillatory blowing (reduced duty cycle), we performed calculations with different frequencies. An overview of these cases is provided in Fig. 9. Shown are isosurfaces of instantaneous spanwise vorticity $\omega_z = \partial v_2/\partial x_1 - \partial v_1/\partial x_2$. As can be observed from the plots, the flow responds to the forcing for a wide range of frequencies. It appears that the forcing is effective in reducing the extent and intensity of the separation although only instantaneous pictures are shown in Fig. 9. A plot of

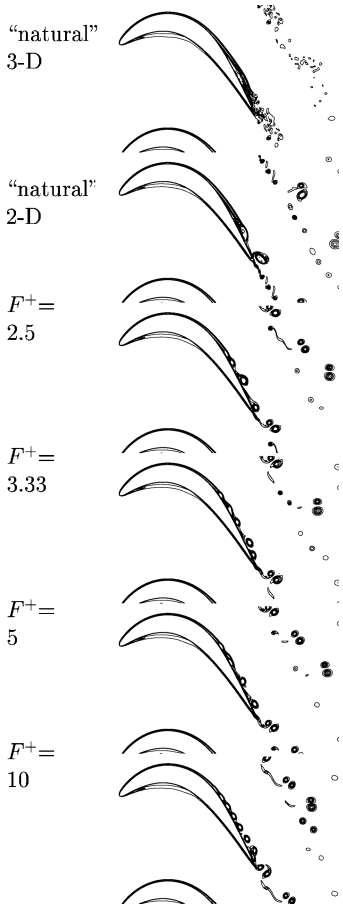

Fig. 9 Isocontours of instantaneous spanwise vorticity ω_z. The three-dimensional result was averaged in the spanwise direction; natural (uncontrolled) flow (three- and two-dimensional calculations) and two-dimensional calculations with pulsed blowing through slot; design blade spacing.

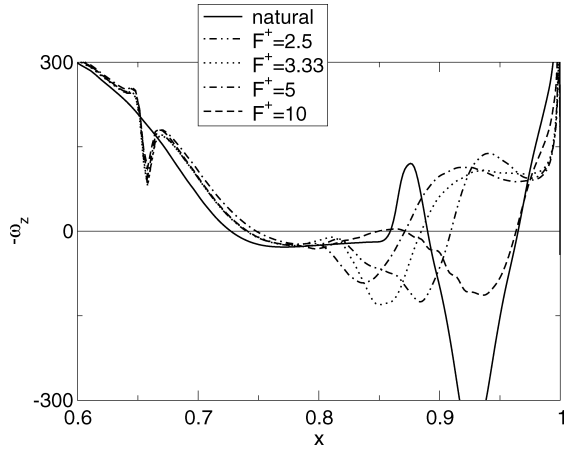

Fig. 10 Time-averaged wall vorticity ω_z on suction side of blade: design blade spacing.

the time-averaged wall vorticity (Fig. 10) helps identify the mean locations of separation and reattachment. In the uncontrolled case the flow separates at $x \approx 0.73C_x$ and reattaches at $x \approx 0.97C_x$. A small secondary separation bubble forms at $0.86 \leq x/C_x \leq 0.89$. Figure 11 shows space/time diagrams of the wall vorticity for the uncontrolled case and a controlled case. Light shaded areas represent regions of low wall shear stress. In the uncontrolled case, strongly time periodic spanwise structures develop downstream of $0.87C_x$. When the wall vorticity is Fourier transformed in time, the periodicity of the shedding becomes visible as a pronounced amplitude peak at $F^+ \approx 3.3$ (Fig. 12). Each forcing pulse also generates an upstream traveling acoustic wave that is visible in the space/time diagrams. When the flow control is applied, separation is delayed (Fig. 10). Because a reduced duty cycle (square forcing function) is employed, higher harmonics are automatically forced as well (see

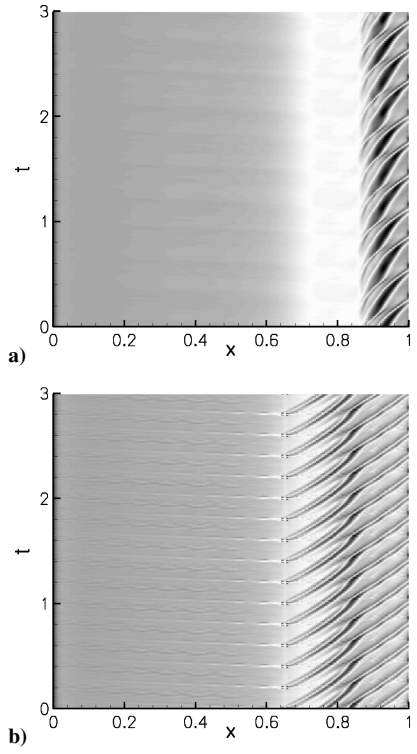

Fig. 11 Time evolution of wall vorticity ($\omega_z = -1200 \ldots 1200$) on suction side of blade for a) natural (uncontrolled) and b) controlled ($F^+ = 5$) cases: design blade spacing.

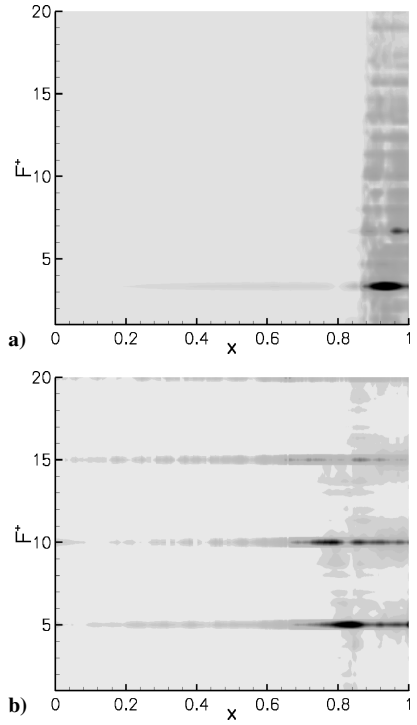

Fig. 12 Fourier transform of wall vorticity on suction side of blade [$A(\omega_z) = 0 \ldots 400$] for a) natural (uncontrolled) and b) controlled ($F^+ = 5$) cases: design blade spacing.

Fig. 3). The pressure distributions of the controlled cases approach the prediction obtained from an Euler method[8] (Fig. 8) indicating that the flow control is very effective and almost completely prevents separation. The frequency spectra for the controlled cases are less broad than for the natural (uncontrolled) case (e.g., see Fig. 12). The dominant frequencies can easily be obtained from a Fourier transform of either one of the aerodynamic coefficients (Fig. 13). When the flow is forced with $F^+ = 10$, the separated shear layer is

Table 3 Time averages and standard deviations σ of aerodynamic coefficients c_x and c_y; ratio of aerodynamic coefficients and its percentage change (gain) with respect to the natural (uncontrolled) case; natural (uncontrolled) case (top) and controlled cases for four different forcing frequencies F^+; design blade spacing

F^+	c_x	$\sigma(c_x)$	c_y	$\sigma(c_y)$	c_y/c_x	Gain, %
——	1.595	0.145	2.885	0.109	1.809	——
2.5	1.442	0.153	2.795	0.247	1.938	7.1
3.33	1.444	0.166	2.792	0.158	1.934	6.9
5	1.434	0.133	2.794	0.120	1.948	7.7
10	1.486	0.200	2.818	0.145	1.896	4.8

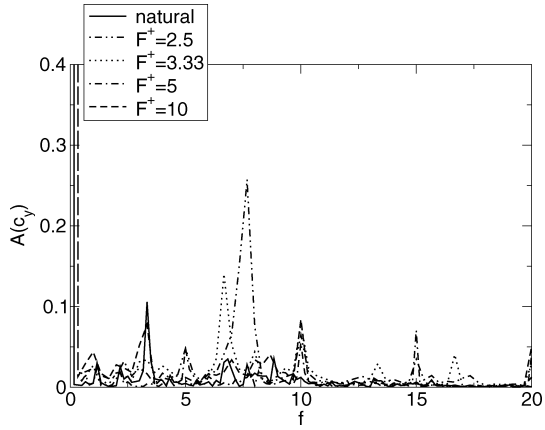

Fig. 13 Fourier transform of aerodynamic coefficient c_y: design blade spacing.

first dominated by $F^+ = 10$. Close to the trailing edge the subharmonic $F^+ = 3.3$ surpasses the fundamental ($F^+ = 10$) in amplitude. This process can be interpreted as vortex merging possibly due to a subharmonic resonance. When the flow is forced with $F^+ = 3.33$, it is dominated by the higher harmonic $F^+ = 6.67$; when the flow is forced with $F^+ = 2.5$, the higher harmonic $F^+ = 7.5$ is generated. The frequency for which the disturbances are most amplified appears to be close to $F^+ = 7.5$. If the flow were forced at this frequency, the flow control would be most efficient, requiring the least energy input. This optimum frequency is considerably higher than the dominant frequency of the uncontrolled flow, $F^+ = 3.3$. As one might expect, the frequency that the flow is most unstable to is related to the inverse of the separation bubble length. On the other hand, forcing at the optimal frequency can lead to very large dynamic aerodynamic loads on the blade. Of the various cases discussed here, forcing with $F^+ = 5$ resulted in the smallest separated flow region (Fig. 10).

Time-averaged aerodynamic coefficients for the various forcing cases in comparison with the natural (uncontrolled) case are listed in Table 3. The three-dimensional results are not included because the computed time interval was too short for obtaining reasonable time averages. For all controlled cases, a gain in c_y/c_x is obtained. A visual representation of the results in Table 3 is given in Fig. 14.

25% Larger Blade Spacing

With a blade spacing of $d/C_x = 1.1$ (that is, an increase of 25% compared to the design spacing), the separated region, and hence the performance losses, are much larger. The area enclosed by the c_p curves (Fig. 15) is larger than for the design blade spacing (Fig. 8) because each individual blade has to exert a larger aerodynamic force on the flow. Instantaneous spanwise vorticity contours are shown in Fig. 16. The difference between the two- and three-dimensional calculations is more pronounced than for the design blade spacing. In the three-dimensional simulation the flow separates somewhat earlier than in the two-dimensional simulation. The hump in the c_p curve of the two-dimensional calculation

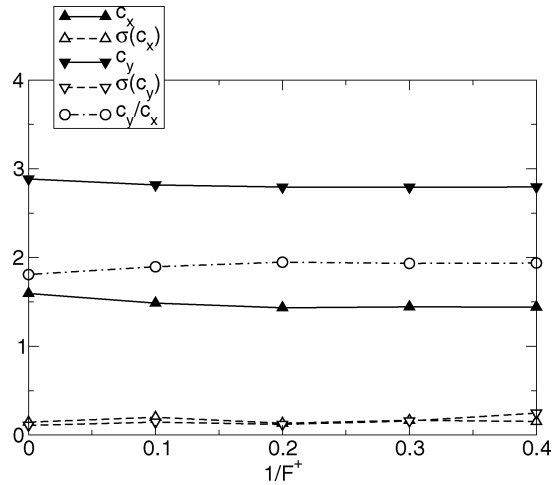

Fig. 14 Time averages and standard deviations σ of aerodynamic coefficients c_x and c_y. $1/F^+ = 0$ result is for natural (uncontrolled) case: design blade spacing.

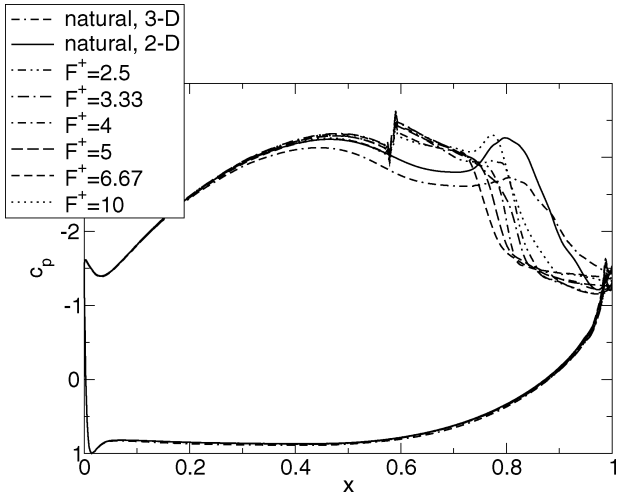

Fig. 15 Time-averaged wall-pressure coefficient: 25% larger blade spacing.

is far less pronounced for the three-dimensional simulation indicating significantly weaker spanwise coherent structures when compared with the two-dimensional calculation. A visualization of the instantaneous three-dimensional flowfield reveals turbulent eddies for $x > 0.8$ (Fig. 17). The assumption made earlier, that two-dimensional calculations capture the relevant aspects of the flow, was based on the observation from the design blade spacing that the turbulent motion was mostly confined to the trailing edge and the wake. As mentioned earlier, three-dimensional simulations are too expensive at this moment for AFC parameter studies. Therefore, to allow for a comparison with the results obtained for the design blade spacing, the feasibility of AFC by pulsed blowing for the 25% larger blade spacing is again demonstrated in two-dimensional calculations.

Figure 18 shows space/time diagrams of the wall vorticity for the uncontrolled case and three controlled cases. The natural (uncontrolled) flow shows little periodicity and a very broad frequency spectrum for the wall vorticity (Fig. 19). More energy is contained in the lower-frequency range of the spectrum than for the design blade spacing. This is not surprising because the separation bubble and the associated length scales are larger than for the design blade spacing. In the uncontrolled case, massive boundary-layer separation occurs on the suction side of the blade, starting at $0.62C_x$ (Fig. 20). The flow reattaches at $0.97C_x$. For all of the controlled cases separation is reduced considerably (Fig. 20). The shortest separated flow region is obtained when the flow is forced with $F^+ = 6.67$. For this forcing

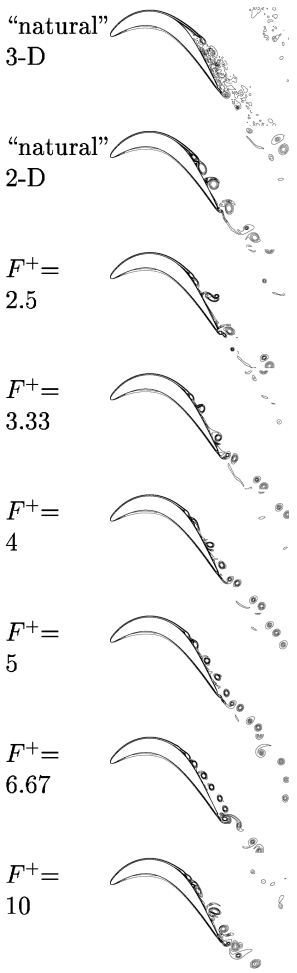

Fig. 16 Isocontours of instantaneous spanwise vorticity ω_z. The three-dimensional result was averaged in the spanwise direction; natural (uncontrolled) flow (three- and two-dimensional calculations) and two-dimensional calculations with pulsed blowing through slot; 25% larger blade spacing.

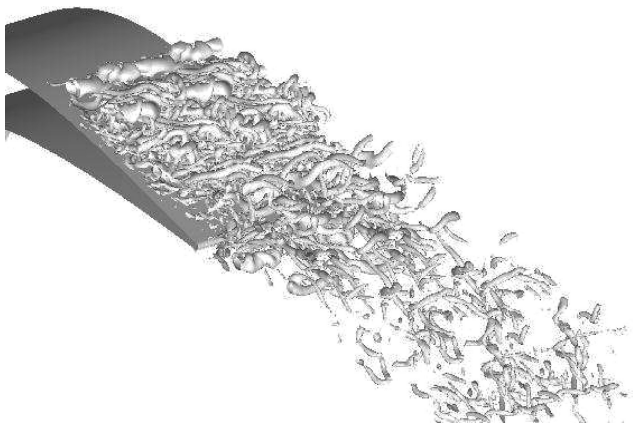

Fig. 17 Isosurface of $Q = 1000$ for three-dimensional simulation: perspective view in upstream direction; 25% larger blade spacing.

frequency the introduced disturbances are most amplified (Fig. 21). Disturbances at higher frequencies experience larger amplification rates closer to the forcing slot where the boundary layer is thinner. Interestingly, forcing with $F^+ = 6.67$ does also have a strong upstream influence (notice the large disturbance amplitude for this case close to $x \approx 0$). Apparently, the total circulation oscillates with the forcing frequency. For forcing with $F^+ = 6.67$, the wall vorticity fluctuations become periodic, and a very pronounced peak appears in the frequency spectrum (Fig. 22). A similar effect is obtained when the flow is forced at the subharmonic frequency, $F^+ = 3.33$. When the flow "locks in" to the forcing, as, for example, for $F^+ = 3.33$ and $F^+ = 6.67$, the largest gain in aerodynamic performance is achieved

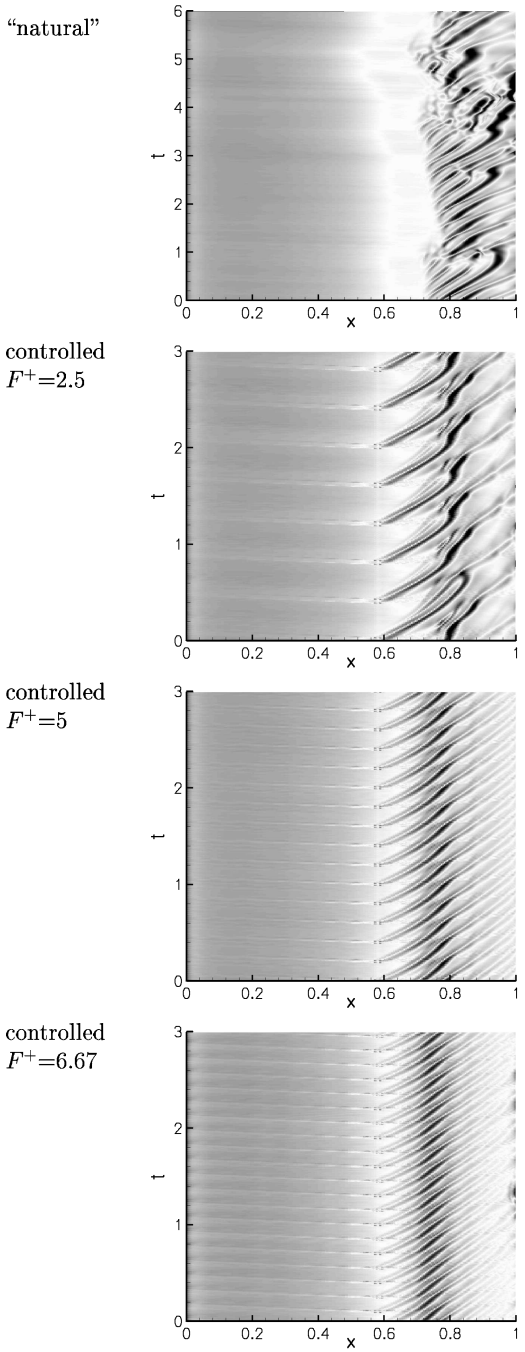

Fig. 18 Time evolution of wall vorticity on suction side of blade ($\omega_z = -1200...1200$) for natural (uncontrolled) and controlled cases; 25% larger blade spacing.

(Table 4 and Fig. 23). However, the dynamic aerodynamic loads on the blade can become very large. When the flow is forced with $F^+ = 5$ (a frequency that is slightly lower than the most amplified frequency), the dynamic load is considerably reduced. For this case the fundamental ($F^+ = 5$) and higher harmonic ($F^+ = 10$) are both close to $F^+ = 6.67$ and are both amplified. The amplification rates are, however, weaker than when the flow is forced with $F^+ = 6.67$. Nevertheless, the loss in aerodynamic performance because of this compromise is very small (Fig. 23). When the flow is forced with $F^+ = 2.5$, the frequency spectrum becomes broader again. The higher harmonic disturbances, for example, $F^+ = 5$ and 7.5, grow less rapidly than when being forced separately.

As observed in Table 4 and Fig. 23, the gain in aerodynamic performance clearly depends on the forcing frequency. As a result of the flow control, the time-averaged ratio of lift and drag is increased

Table 4 Time-averages and standard deviations σ of aerodynamic coefficients c_x and c_y; ratio of aerodynamic coefficients and its percentage change (gain) with respect to the natural (uncontrolled) case; natural (uncontrolled) case (top) and controlled cases for six different forcing frequencies F^+; 25% larger blade spacing

F^+	c_x	$\sigma(c_x)$	c_y	$\sigma(c_y)$	c_y/c_x	Gain, %
——	1.424	0.234	3.156	0.190	2.216	——
2.5	1.227	0.315	3.095	0.280	2.522	13.8
3.33	1.199	0.207	3.090	0.752	2.577	16.3
4	1.191	0.129	3.082	0.152	2.588	16.8
5	1.161	0.153	3.053	0.192	2.630	18.7
6.67	1.142	0.158	3.021	0.764	2.645	19.4
10	1.315	0.185	3.129	0.181	2.379	7.4

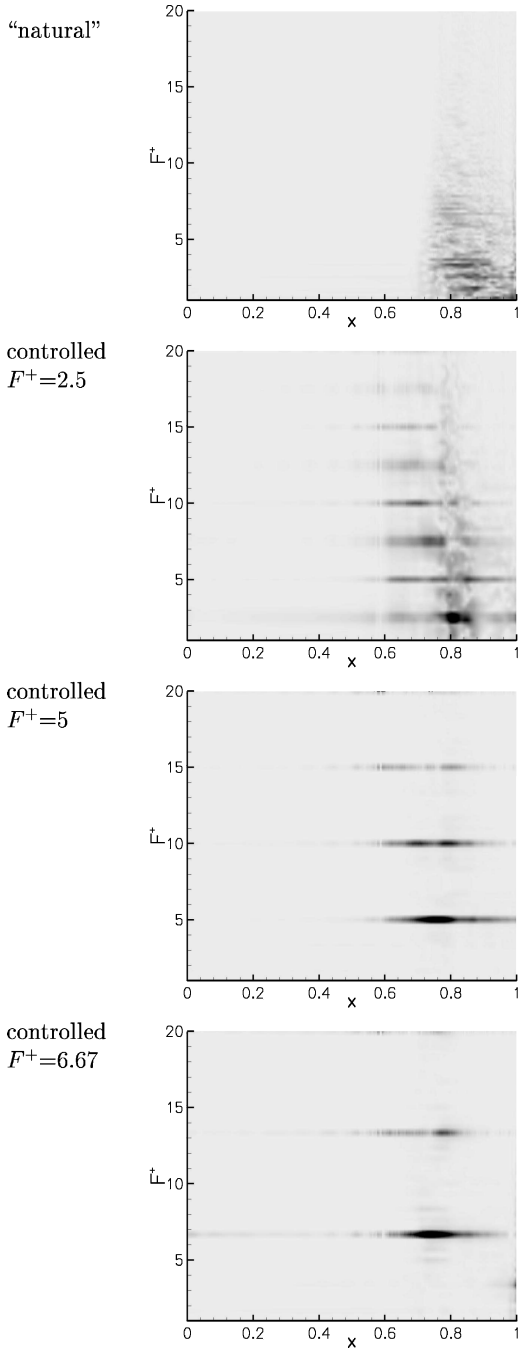

Fig. 19 Fourier transform of wall vorticity on suction side of blade [$A(\omega_z) = 0...400$] for natural (uncontrolled) and controlled cases; 25% larger blade spacing.

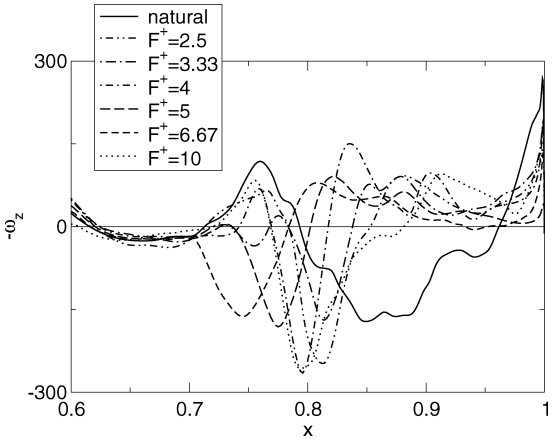

Fig. 20 Time-averaged wall vorticity ω_z on suction side of blade; 25% larger blade spacing.

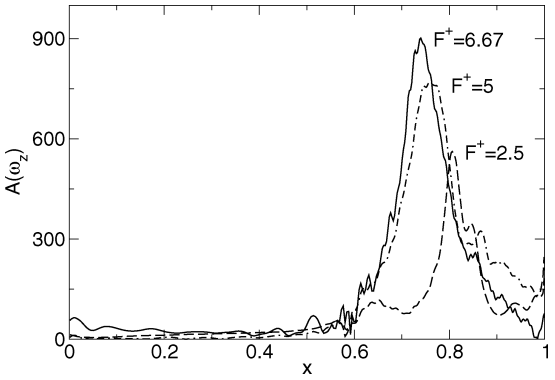

Fig. 21 Amplitude of the fundamental disturbance (same frequency as the forcing) for three different forcing frequencies. Amplitudes were obtained from Fourier transform of wall vorticity.

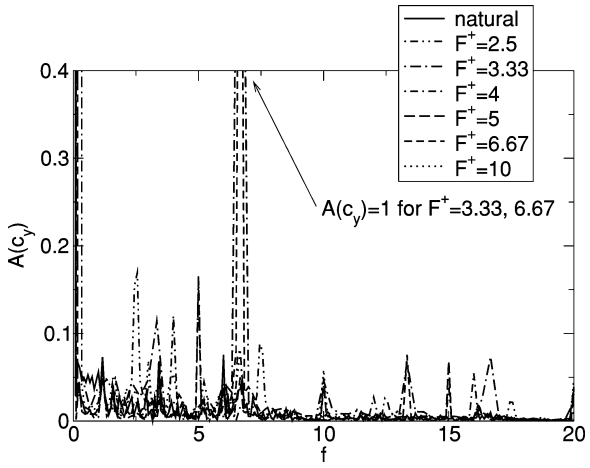

Fig. 22 Fourier transform of aerodynamic coefficient c_y; 25% larger blade spacing.

by as much as 19.4% for forcing with $F^+ = 6.67$. The increase in lift over drag of the controlled cases can be associated with a larger circulation and a smaller time-averaged separation bubble (Fig. 24) when compared with the uncontrolled case. Profiles of time-averaged wall-tangential velocity for five different downstream stations (Fig. 4) are shown in Fig. 25. For the controlled cases spanwise structures that add to the mixing in wall-normal direction appear farther upstream than for the uncontrolled case (also see Fig. 18). Although the bubble thickness is larger at $x = 0.73C_x$ when the flow is forced with $F^+ = 10$ than for all other forcing frequencies, the fullest profile at $x = 0.84C_x$ is obtained with $F^+ = 4$,

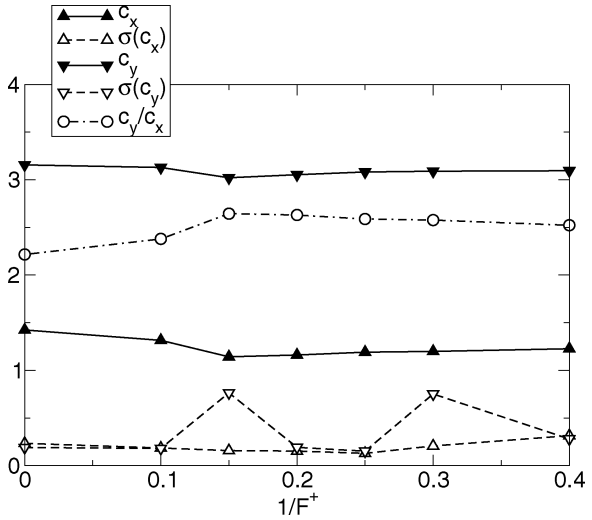

Fig. 23 Time averages and standard deviations σ of aerodynamic coefficients c_x and c_y. $1/F^+ = 0$ result is for natural (uncontrolled) case; 25% larger blade spacing.

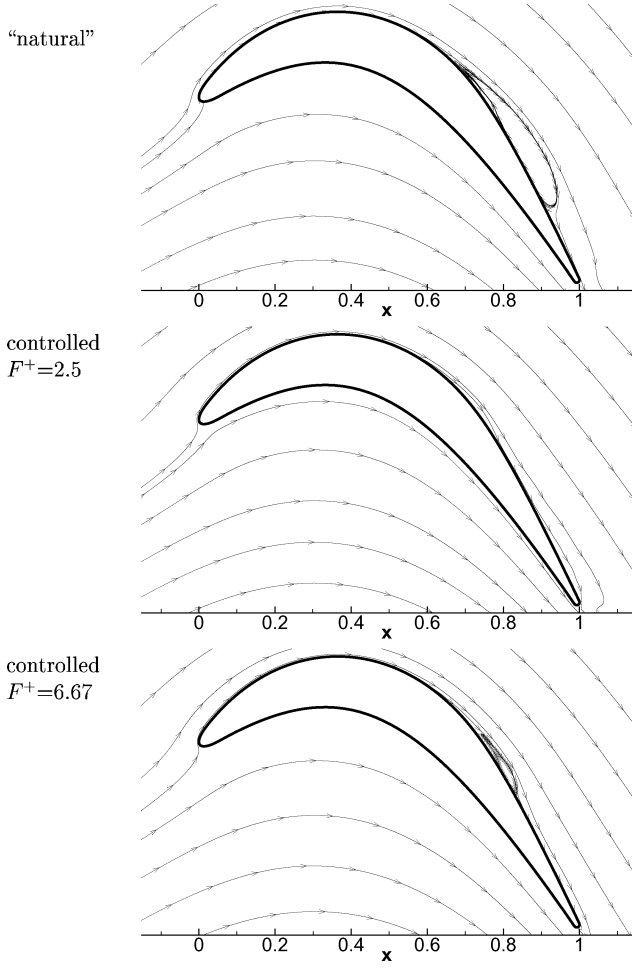

Fig. 24 Time-averaged streamlines for natural (uncontrolled) and controlled cases; 25% larger blade spacing.

and the fullest profile at $x = 0.92C_x$ is obtained with $F^+ = 2.5$. The best wall-normal momentum transfer in the upstream part of the separation bubble is achieved when the flow is forced at high frequencies; the best mixing in the downstream part is achieved when the flow is forced at low frequencies. The local optimum forcing frequency appears to be inversely proportional to the local bubble thickness. If the forcing frequency is chosen too high (here $F^+ = 10$), the flow control loses effectiveness.

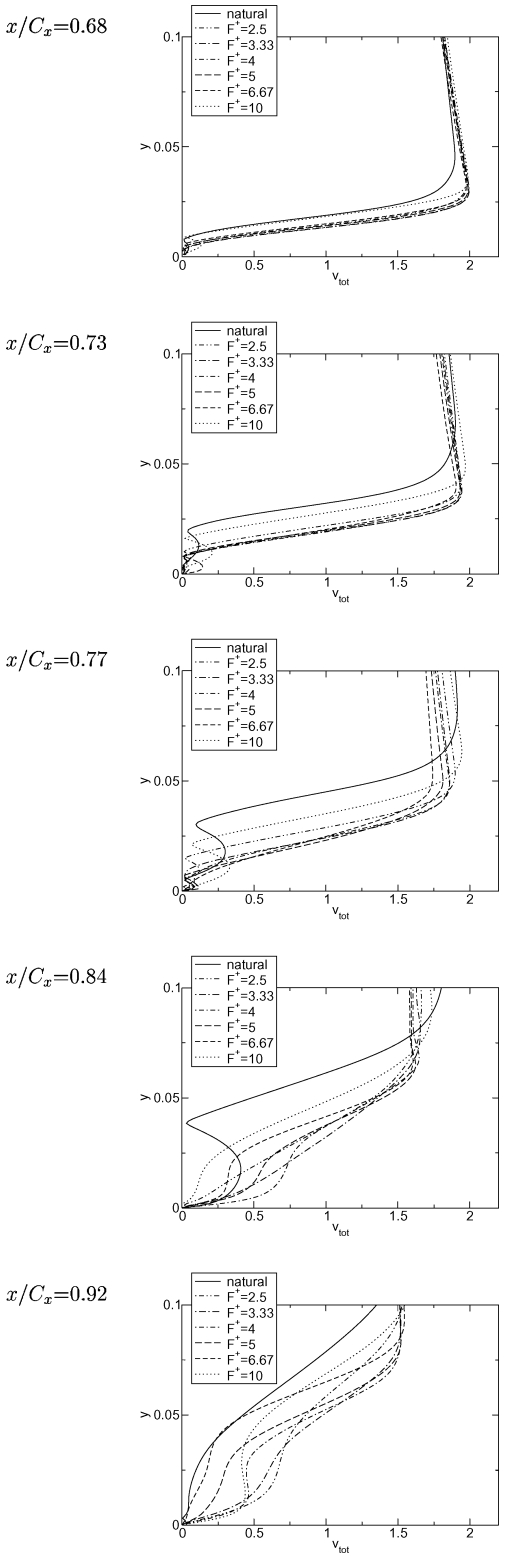

Fig. 25 Profiles of time-averaged wall-tangential velocity; 25% larger blade spacing.

Summary

Laminar separation in low-pressure turbine (LPT) stages can lead to significant performance losses. Active flow control (AFC) by pulsed vortex generator jets (VGJs) for preventing laminar separation in a PakB LPT cascade was tested in experiments by Rivir and coworkers (see Refs. 1–5). For our LPT flow simulations we chose the same blade geometry and inflow conditions as in the experiments. Simulations were performed for the design blade spacing and for a 25% larger blade spacing. Results obtained from two- and three-dimensional simulations at the design blade spacing were compared with the experimental data. In the simulations the extent and intensity of the separation were consistently underpredicted. The reasons for the systematic discrepancies between the experiment and the calculations are still not understood. At the design blade spacing turbulent motion was mainly confined to the trailing wake. At the 25% larger blade spacing the flow transitions well upstream of the trailing edge and thus has a larger effect on the separation location. For the larger spacing, no experimental data were available for comparison with the numerical results. It was found that the strength of two-dimensional structures was overpredicted in two-dimensional simulations, resulting in strong wall-normal mixing delaying separation. The coherence of the spanwise structures was shown to be weakened in three-dimensional simulations resulting in a larger separated flow. We conjecture that the remaining discrepancies between experiment and the three-dimensional simulations might be caused by inflow turbulence, wall roughness, and insufficient grid resolution of the three-dimensional simulations.

AFC by means of pulsed blowing through a slot was explored in two-dimensional simulations. The duty cycle was $\tau = 10\%$, and the blowing ratio was $B = 2$. Forcing with a reduced duty cycle (square forcing function) was shown to simultaneously introduce the fundamental of the forcing frequency and its higher harmonics. With pulsed blowing an 8% increase in lift over drag could be achieved for the design blade spacing and an increase of 19% could be achieved for the 25% larger spacing. The effectiveness of AFC by pulsed actuation appears to be related to the hydrodynamic instability mechanisms inherent in the flow. The separated shear layer is unstable with regard to two-dimensional disturbances. Pulsed blowing through a slot results in the formation of energetic, two-dimensional, spanwise coherent structures. These structures delay separation and/or aid in reattaching the flow by increasing the momentum exchange between the freestream and the boundary layer. When the flow was forced at a frequency that resulted in a maximum amplification of the introduced disturbances, the control became most effective. However, forcing at this frequency also led to large dynamic aerodynamic loads. When the forcing frequency was only slightly offset from this frequency, similar performance gains were achieved with much lower dynamic loads. It should be kept in mind that the parameter space for AFC is very large. Different forcing functions $f(t)$, blowing ratios B, and duty cycles τ need to be explored for finding a control with minimum energy input. Finally, for numerical simulations to provide additional insight contributing to the experimental effort of controlling laminar separation by pulsed VGJs, three-dimensional simulations resolving the VGJ dynamics in time and space have to be performed.

Acknowledgments

This work was supported by the Air Force Office of Scientific Research under Grant F49620-02-1-0122 with Thomas J. Beutner serving as Program Manager.

References

[1]Bons, J. P., Sondergaard, R., and Rivir, R. B., "Control of Low-Pressure Turbine Separation Using Vortex Generator Jets," AIAA Paper 99-0367, Jan. 1999.

[2]Bons, J. P., Sondergaard, R., and Rivir, R. B., "Turbine Separation Control Using Pulsed Vortex Generator Jets," *Journal of Turbomachinery*, Vol. 123, No. 2, 2001, pp. 198–206.

[3]Bons, J. P., Sondergaard, R., and Rivir, R. B., "The Fluid Dynamics of LPT Blade Separation Control Using Pulsed Jets," *Journal of Turbomachinery*, Vol. 124, No. 1, 2002, pp. 77–85.

[4]Sondergaard, R., Bons, J. P., and Rivir, R. B., "Control of Low-Pressure Turbine Separation Using Vortex Generator Jets," *Journal of Propulsion and Power*, Vol. 18, No. 4, 2002, pp. 889–895.

[5]Sondergaard, R., Bons, J. P., Sucher, M., and Rivir, R. B., "Reducing Low-Pressure Turbine Stage Blade Count Using Vortex Generator Jet Separation Control," *Proceedings of ASME Turbo Expo 2002*, Vol. 5B, American Society of Mechanical Engineers, New York, 2002, pp. 1055–1061.

[6]Morkovin, M. V., "The Many Faces of Transition," *Viscous Drag Reduction*, edited by C. S. Wells, Plenum, New York, 1969, pp. 1–31.

[7]Lake, J. P., King, P. I., and Rivir, R. B., "Reduction of Separation Losses on a Turbine Blade with Low Reynolds Number," AIAA Paper 99-0242, Jan. 1999.

[8]Huang, J., Corke, T., and Thomas, F., "Plasma Actuators for Separation Control of Low Pressure Turbine Blades," AIAA Paper 2003-1027, Jan. 2003.

[9]Rizzetta, D. P., and Visbal, M. R., "Numerical Investigations of Transitional Flow Through a Low-Pressure Turbine Cascade," AIAA Paper 2003-3587, June 2003.

[10]Rizzetta, D. P., and Visbal, M. R., "Numerical Simulation of Separation Control for Transitional Highly Loaded Low-Pressure Turbines," *AIAA Journal*, Vol. 43, No. 9, 2005, pp. 1958–1967.

[11]Postl, D., Gross, A., and Fasel, H. F., "Numerical Investigation of Low-Pressure Turbine Blade Separation Control," AIAA Paper 2003-0614, Jan. 2003.

[12]Postl, D., Gross, A., and Fasel, H. F., "Numerical Investigation of Active Flow Control for Low-Pressure Turbine Blade Separation," AIAA Paper 2004-0750, Jan. 2004.

[13]Gross, A., and Fasel, H. F., "Active Flow Control of Separation for Low-Pressure Turbine Blades," AIAA Paper 2004-2203, June–July 2004.

[14]Mutnuri, P. K., Ayyalasomayajula, H., Ghia, U., and Ghia, K., "Analysis of Separated Flow in a Low-Pressure Turbine Cascade, Using Multi-Block Structured Grid," AIAA Paper 2003-0793, Jan. 2003.

[15]Raverdy, B., Mary, I., and Sagaut, P., "High-Resolution Large-Eddy Simulation of Flow Around Low-Pressure Turbine Blade," *AIAA Journal*, Vol. 41, No. 3, 2003, pp. 390–397.

[16]Michelassi, V., Wissink, J. G., Fröhlich, J., and Rodi, W., "Large-Eddy Simulation of Flow Around Low-Pressure Turbine Blade with Incoming Wakes," *AIAA Journal*, Vol. 41, No. 11, 2003, pp. 2143–2156.

[17]Xiaohua, W., and Durbin, P. A., "Evidence of Longitudinal Vortices Evolved from Distorted Wakes in a Turbine Passage," *Journal of Fluid Mechanics*, Vol. 446, 2001, pp. 199–228.

[18]Suzen, Y. B., and Huang, P. G., "Numerical Simulation of Transitional Flows as Affected by Passing Wakes," AIAA Paper 2004-0103, Jan. 2004.

[19]Gross, A., and Fasel, H., "High-Order WENO Schemes Based on the Roe Approximate Riemann Solver," AIAA Paper 2002-2735, June 2002.

[20]Margolin, L. G., and Rider, W. J., "A Rationale for Implicit Turbulence Modeling," *International Journal for Numerical Methods in Fluids*, Vol. 39, 2002, pp. 821–841.

[21]Fasel, H. F., and Postl, D., "Interaction of Separation and Transition in Boundary Layers: Direct Numerical Simulations," *Laminar-Turbulent Transition, Proceedings of the IUTAM Symposium*, Springer (to be published).

[22]Hunt, J. C. R., Wray, A. A., and Moin, P., "Eddies, Stream, and Convergence Zones in Turbulent Flows," Center for Turbulence Research, Proc. CTR Summer Program, Stanford Univ., Stanford, CA, 1988, pp. 193–208.

H. Reed
Associate Editor